

pubs.acs.org/journal/apchd5 Article

Green Tensor Analysis of Lattice Resonances in Periodic Arrays of Nanoparticles

Lauren Zundel, Alvaro Cuartero-González, Stephen Sanders, Antonio I. Fernández-Domínguez, and Alejandro Manjavacas*



Cite This: ACS Photonics 2022, 9, 540-550



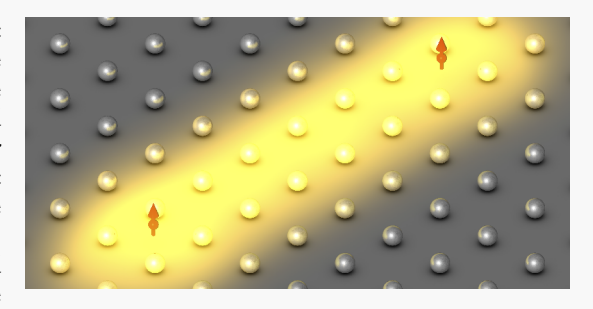
ACCESS

III Metrics & More



Supporting Information

ABSTRACT: When arranged in a periodic geometry, arrays of metallic nanostructures are capable of supporting collective modes known as lattice resonances. These modes, which originate from the coherent multiple scattering between the elements of the array, give rise to very strong and spectrally narrow optical responses. Here, we show that, thanks to their collective nature, the lattice resonances of a periodic array of metallic nanoparticles can mediate an efficient long-range coupling between dipole emitters placed near the array. Specifically, using a coupled dipole approach, we calculate the Green tensor of the array connecting two points and analyze its spectral and spatial characteristics. This quantity represents the electromagnetic field produced by the array at a given position when excited



by a unit dipole emitter located at another one. We find that, when a lattice resonance is excited, the Green tensor is significantly larger and decays more slowly with distance than the Green tensor of vacuum. Therefore, in addition to advancing the fundamental understanding of lattice resonances, our results show that periodic arrays of nanostructures are capable of enhancing the long-range coupling between collections of dipole emitters, which makes them a promising platform for applications such as nanoscale energy transfer and quantum information processing.

KEYWORDS: lattice resonances, periodic arrays, nanoparticle arrays, Green tensor, dipole-dipole coupling, quantum emitters

Lattice resonances are collective modes supported by periodic arrays of nanostructures that originate from the coherent multiple scattering between the individual array constituents. These resonances appear in the spectrum at wavelengths commensurate with the periodicity of the array and, due to their collective nature, produce optical responses that are simultaneously very strong and spectrally narrow, thus leading to record quality factors for metallic systems. 16-25 Thanks to these exceptional properties, periodic arrays of metallic nanostructures are being used in a broad range of applications. These include the implementation of ultrasensitive sensors, 26-29 the development of platforms for exploring new physical phenomena, 30-34 as well as the design of different optical elements, such as light-emitting devices, 35-46 lenses, 47 color filters, 48-50 and nonlinear devices. 51-54

Interestingly, in the majority of these applications, the lattice resonances are excited from the far-field using a propagating electromagnetic wave, such as a collimated laser. As a consequence, most of the theoretical characterization of the optical properties of periodic arrays of metallic nanostructures has been focused on describing their far-field response through the analysis of quantities such as the reflectance, transmittance, and absorbance. However, lattice resonances also produce very large electromagnetic fields around the array, 55-58 which, as we have recently shown, are ultimately limited by the

number of elements of the array that interact coherently.⁵⁹ The strong near-fields provided by lattice resonances play a crucial role for applications, such as nanolasing, in which the arrays interact with quantum emitters placed in their vicinity.^{37,60,61} Specifically, in these systems, the lattice resonances couple with the emitters (usually quantum dots or dye molecules) that constitute the gain medium and provide the necessary feedback to achieve lasing.^{44,45,62–68} These modes can also strongly influence the emission patterns of the emitters.^{69,70} Furthermore, the collective character of lattice resonances and their extended nature makes them ideal candidates to provide an efficient long-range interaction between emitters placed near the array. This possibility has started to be explored to achieve collective emission,^{71,72} as well as long-range energy propagation⁷³ and dipole—dipole coupling.⁷⁴

In this Article, motivated by the recent experimental advances, we provide a detailed theoretical investigation of the coupling between dipole emitters mediated by the lattice

Received: September 23, 2021 Published: January 14, 2022





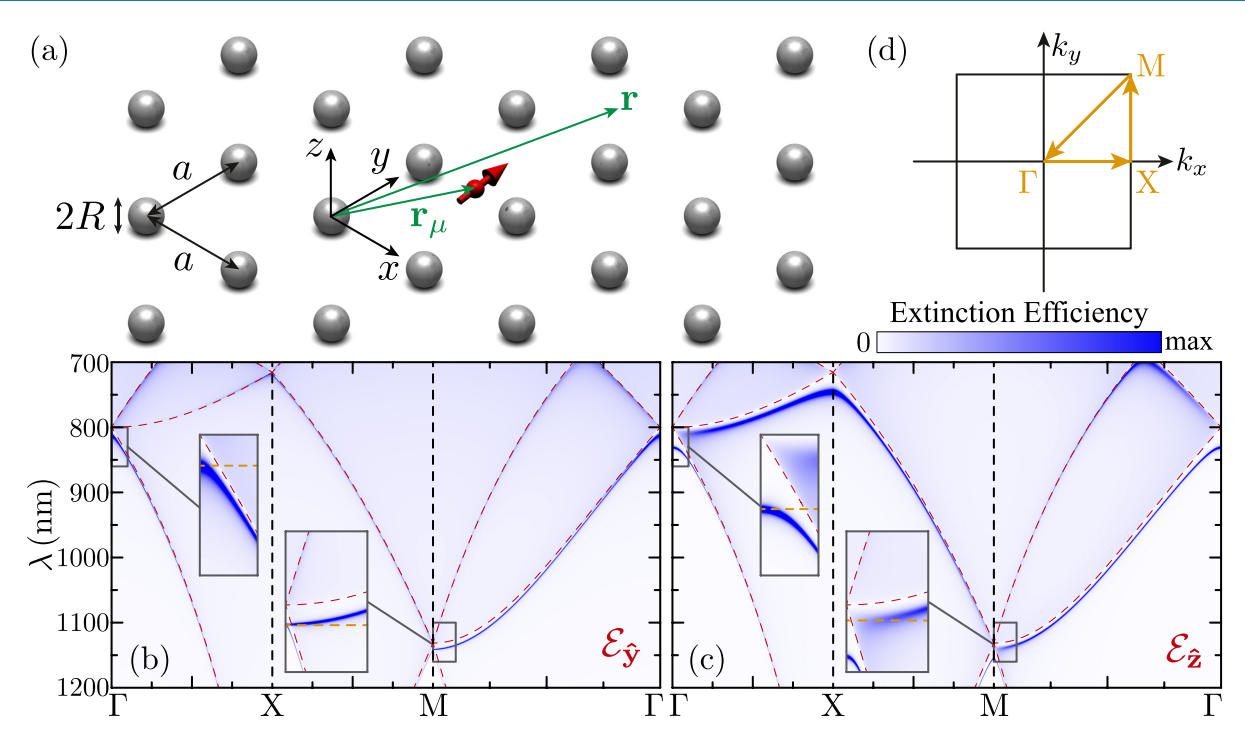


Figure 1. (a) Schematics of the system under study, consisting of a square array of period a made of identical silver nanospheres with radius R. The array is located in the xy-plane and is surrounded by vacuum. We are interested in the analysis of the Green tensor of the array connecting two points \mathbf{r}_{μ} and \mathbf{r} , which represents the field produced by the array at $\mathbf{r} = (x, y, z)$ when excited by a unit dipole located at $\mathbf{r}_{\mu} = (x_{\mu}, y_{\mu}, z_{\mu})$. (b, c) Dispersion diagrams showing the extinction efficiency of an array with a = 800 nm and R = 100 nm for y (b) and z (c) polarizations (see eq 2), calculated along the path in the first Brillouin zone depicted in (d). The red dashed curves in panels (b) and (c) indicate the position of the Rayleigh anomalies, while the insets show zooms of relevant regions of the dispersion relations, with the yellow dashed lines marking the onset and cutoff of the lowest-order lattice resonance at the Γ and M points, respectively.

resonances supported by periodic arrays of metallic nanoparticles. To that end, we implement a theoretical approach based on the coupled dipole model that allows us to compute the Green tensor of the array connecting two points \mathbf{r}_u and \mathbf{r} . This quantity, which represents the electromagnetic field produced by the array at r when excited by a unit dipole located at \mathbf{r}_{uv} completely describes the optical response of the array. Using this approach, we analyze the spectral and spatial characteristics of the Green tensor of the array and show that, when a lattice resonance is excited, this quantity is largely enhanced with respect to the Green tensor of vacuum and decays with $|\mathbf{r} - \mathbf{r}_{\mu}|$ at a much slower rate. Therefore, in addition to describing and implementing a powerful approach to investigate the near-field excitation of lattice resonances by localized sources, we provide a comprehensive analysis of how these collective modes can enhance the long-range coupling between dipole emitters and unravel the physical mechanisms behind that effect. Our results constitute a solid theoretical framework that facilitates the interpretation of recent experimental results, 71-74 as well as the development of new applications exploiting the exceptional optical properties of periodic arrays of nanoparticles.

RESULTS AND DISCUSSION

The system under study, which is depicted in Figure 1a, consists of a square array with period a made of identical silver nanospheres of radius R. The array is located in the xy-plane and surrounded by vacuum. We assume that R is significantly smaller than both a and the wavelength of light λ , which allows us to characterize the response of the array using a coupled dipole model. 1,3,19,75-77 Within this approximation, we model

each of the nanoparticles of the array as a point dipole with both electric \mathbf{p} and magnetic \mathbf{m} components, whose responses are characterized by an electric α^E and a magnetic α^M polarizability, respectively. Although, in this work, we focus on metallic nanoparticles, for which the magnetic polarizability plays a minor role, we have opted to include it in the model to ensure the theory is applicable to a wide range of systems. As shown explicitly in the Methods section, the coupled dipole model allows us to derive the following closed expression for the electric and magnetic field produced by the array at a point $\mathbf{r} = (x, y, z)$, when excited by a unit dipole with electric $\hat{\boldsymbol{\mu}}^E$ and magnetic $\hat{\boldsymbol{\mu}}^M$ components, located at $\mathbf{r}_u = (x_u, y_u, z_u)$

$$\begin{bmatrix} \mathbf{E}(\mathbf{r}) \\ \mathbf{B}(\mathbf{r}) \end{bmatrix} = \frac{a^2}{4\pi^2} \int_{1BZ} d\mathbf{k}_{\parallel} \mathcal{G}(\mathbf{k}_{\parallel}, \mathbf{r}) \mathcal{A}(\mathbf{k}_{\parallel}) \mathcal{G}(\mathbf{k}_{\parallel}, -\mathbf{r}_{\mu}) \begin{bmatrix} \hat{\boldsymbol{\mu}}^{E} \\ \hat{\boldsymbol{\mu}}^{M} \end{bmatrix}$$
(1)

Here, 1BZ stands for the first Brillouin zone, $\mathcal{G}(\mathbf{k}_{\parallel}, \mathbf{r})$ is the lattice sum tensor

$$\mathcal{G}(\mathbf{k}_{\parallel}, \mathbf{r}) = \begin{bmatrix} \mathcal{G}^{\text{EE}}(\mathbf{k}_{\parallel}, \mathbf{r}) & \mathcal{G}^{\text{EM}}(\mathbf{k}_{\parallel}, \mathbf{r}) \\ -\mathcal{G}^{\text{EM}}(\mathbf{k}_{\parallel}, \mathbf{r}) & \mathcal{G}^{\text{EE}}(\mathbf{k}_{\parallel}, \mathbf{r}) \end{bmatrix}$$

with its electric–electric and electric–magnetic components explicitly defined in the Methods section, and $\mathcal{A}(\mathbf{k}_{\parallel}) = [\alpha^{-1} - \mathcal{G}(\mathbf{k}_{\parallel}, 0)]^{-1}$ is the polarizability of the array (see eq 8). This last quantity encodes the intrinsic response of the array, which is determined by the interplay between the response of the nanoparticles, described by the polarizability

tensor α , and the geometry of the lattice, contained in the lattice sum tensor $\mathcal{G}(\mathbf{k}_{\parallel}, 0)$.

The integral over \mathbf{k}_{\parallel} in eq 1 is the result of the localized character of the dipole source, which breaks the periodicity of the problem. Importantly, the integrand displays narrow features, associated with the lattice resonances of the array, that make it necessary to use an adaptive integration algorithm⁷⁸ to perform the integral. Furthermore, the lack of periodicity also means that a full numerical solution of Maxwell's equations, using, for instance, a finite element (FEM) or a finite-difference time-domain (FDTD) method, requires performing a similar integration, thus making such computation very challenging.

We begin our analysis by characterizing the response of the array through the calculation of its extinction efficiency, defined as 13,79

$$\mathcal{E}_{\hat{\mathbf{n}}} = \frac{4\pi k}{a^2} \operatorname{Im} \{ \hat{\mathbf{n}} \mathcal{A}^{\text{EE}}(\mathbf{k}_{\parallel}) \hat{\mathbf{n}}^{\dagger} \}$$
 (2)

for polarization along $\hat{\mathbf{n}}$. Here, $\mathcal{A}^{\mathrm{EE}}(\mathbf{k}_{\parallel})$ is the electric–electric component of the polarizability of the array, which is the term that dominates the response of arrays of metallic nanoparticles, such as those analyzed here. Figures 1b and c show, respectively, $\mathcal{E}_{\hat{\mathbf{v}}}$ and $\mathcal{E}_{\hat{\mathbf{z}}}$ for an array with a=800 nm and R= 100 nm, calculated along the path in the first Brillouin zone depicted in panel d. We consider wavelengths in the range from 700 to 1200 nm, well within the validity of the dipole model, as demonstrated in Figure S1 of the Supporting Information. Here and in the remainder of this work, we compute the electric and magnetic components of the polarizability of the nanoparticles from the corresponding dipolar Mie scattering coefficients⁸⁰ with a dielectric function described using a Drude model $\varepsilon(\omega) = \varepsilon_{\infty} - \omega_{\rm p}^2/(\omega^2 + i\gamma\omega)$ with $\varepsilon_{\infty} = 5$, $\hbar\omega_{\rm p} = 8.9$ eV, and $\hbar\gamma = 37$ meV.⁸¹ Examining the results shown in Figure 1b,c, we observe that the array supports different lattice resonances characterized by large values of the extinction efficiency. The lattice resonances appear at slightly larger wavelengths than the Rayleigh anomalies (indicated by the red dashed lines), at which the real part of the lattice sums diverge. In this work, we focus on the lowest-order lattice resonance, which has its onset at the Γ point at a wavelength slightly larger than the array period. Furthermore, it displays a cutoff at the M point at a wavelength slightly larger than $\sqrt{2}a$. These two limits, which are indicated in the insets of Figure 1b,c with yellow dashed lines, play an important role in the behavior of the array as we discuss later. Although, for simplicity, we consider the array to be surrounded by vacuum, our analysis can be readily extrapolated to any other homogeneous dielectric environment. However, as is known, ^{59,82} any asymmetry between the media above and below the array can hinder the lattice resonances.

Equation 1 defines the Green tensor of the array connecting two points \mathbf{r}_u and \mathbf{r} as

$$\mathbf{G}(\mathbf{r}, \mathbf{r}_{\mu}) = \frac{a^2}{4\pi^2} \int_{1BZ} d\mathbf{k}_{\parallel} \mathcal{G}(\mathbf{k}_{\parallel}, \mathbf{r}) \mathcal{A}(\mathbf{k}_{\parallel}) \mathcal{G}(\mathbf{k}_{\parallel}, -\mathbf{r}_{\mu})$$
(3)

Due to its dominant role, in this work, we focus our analysis on the electric-electric component of the Green tensor, which satisfies $\mathbf{E}(\mathbf{r}) = \mathbf{G}^{\mathrm{EE}}(\mathbf{r}, \mathbf{r}_{\mu})\hat{\mu}^{\mathrm{E}}$ or, in other words, represents the electric field produced by the array at \mathbf{r} when excited by a unit electric dipole placed at \mathbf{r}_{μ} . In Figure 2, we plot the spectrum of

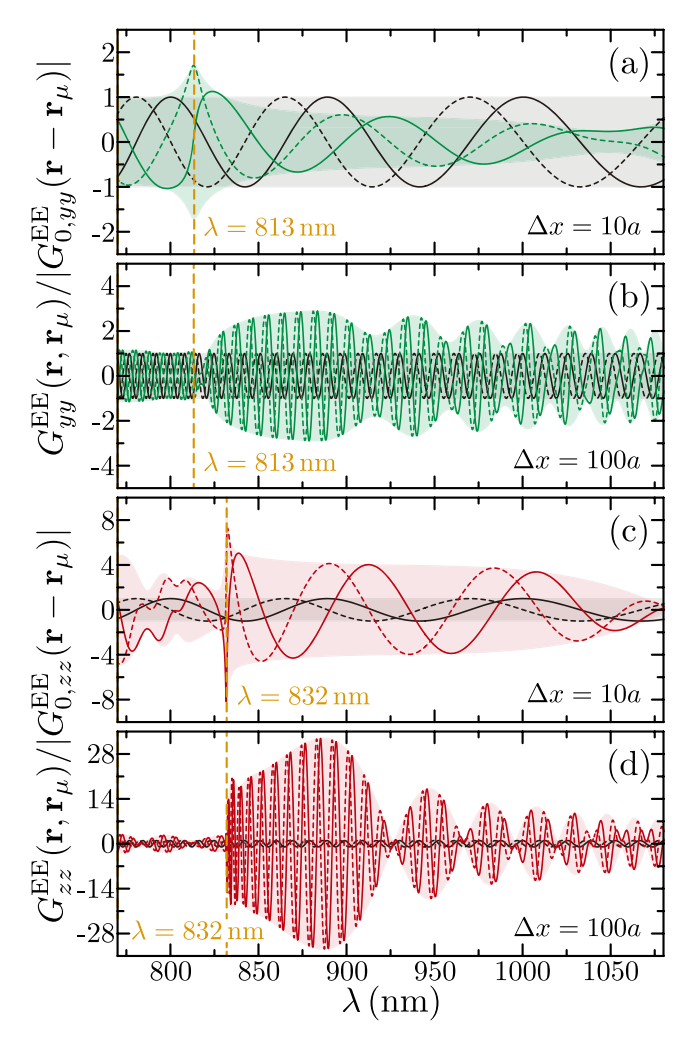


Figure 2. Green tensor of a periodic array with a=800 nm and R=100 nm connecting the points $\mathbf{r}_{\mu}=(0,0,2R)$ and $\mathbf{r}=(\Delta x,0,2R)$. Panels (a) and (b) show the spectrum for the yy component, while panels (c) and (d) display those for the zz component. In both cases, we analyze the results for $\Delta x=10a$ (a, c) and 100a (b, d). The colored solid and dashed curves represent, respectively, the real and imaginary parts of the Green tensor, while the shaded areas indicate its envelope. All of the results are normalized to the amplitude of the same component of the Green tensor of vacuum $\mathbf{G}_0^{\rm EE}(\mathbf{r}-\mathbf{r}_{\mu})$, whose real and imaginary parts are displayed by the black solid curves and whose envelope is signaled by the black shaded areas. In all of the panels, the yellow dashed lines mark the onset of the lattice resonance at the Γ point shown in the insets of Figure 1b,c.

the yy (a, b) and zz components (c, d) of $\mathbf{G}^{\mathrm{EE}}(\mathbf{r}, \mathbf{r}_{\mu})$. We assume $\mathbf{r}_{\mu} = (0, 0, 2R)$ and $\mathbf{r} = (\Delta x, 0, 2R)$, with $\Delta x = 10a$ (a, c) and 100a (b, d) and the same values for the period of the array and the size of the nanoparticles as in Figure 1, that is, a = 800 nm and R = 100 nm. We use colored solid and dashed curves to represent, respectively, the real and imaginary parts of the Green tensor and a color shaded area for its envelope. The results are normalized to the amplitude of the same component of the Green tensor of vacuum $\mathbf{G}_0^{\mathrm{EE}}(\mathbf{r} - \mathbf{r}_{\mu})$ connecting the same two points, which is defined in the Methods section. Notice that this quantity represents the electric field produced at \mathbf{r} by a unit electric dipole placed at \mathbf{r}_{μ} in absence of the array. For this particular configuration, we have $G_{0,yy}^{\mathrm{EE}}(\mathbf{r} - \mathbf{r}_{\mu}) = G_{0,zz}^{\mathrm{EE}}(\mathbf{r} - \mathbf{r}_{\mu}) = \exp(ik\Delta x)[k^2(\Delta x)^2 + ik\Delta x - 1]/(\Delta x)^3$, with $k = 2\pi/\lambda$. We plot the real and imaginary

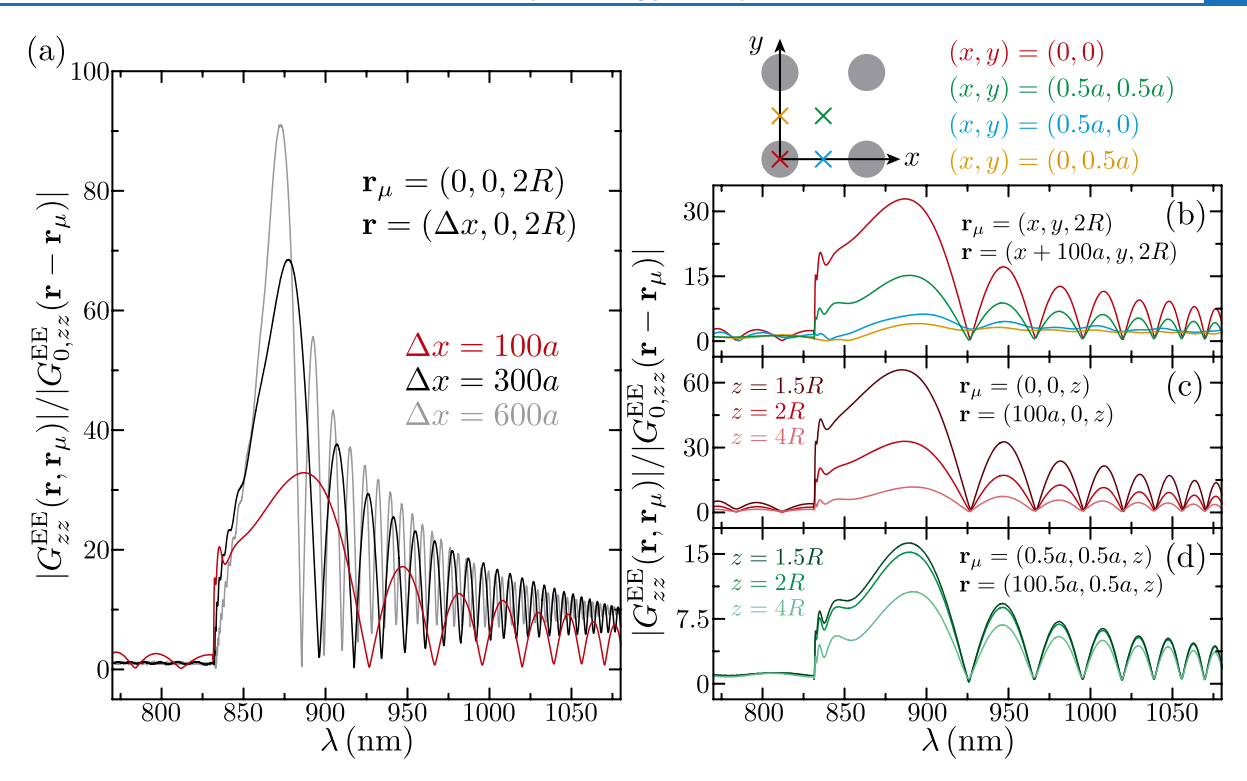


Figure 3. Amplitude of the zz component of the Green tensor of a periodic array with a=800 nm and R=100 nm connecting the points \mathbf{r}_{μ} and \mathbf{r} . Panel (a) shows the spectrum for $\mathbf{r}_{\mu}=(0,0,2R)$ and $\mathbf{r}=(\Delta x,0,2R)$, with $\Delta x=100a$ (red curve), 300a (black curve), and 600a (gray curve). Panel (b) shows the spectrum for $\mathbf{r}_{\mu}=(x,y,2R)$ and $\mathbf{r}=(x+100a,y,2R)$, with the four different combinations of x and y indicated in the upper schematics. Panels (c) and (d) show, respectively, the spectrum for the cases with $\mathbf{r}_{\mu}=(0,0,z)$, $\mathbf{r}=(100a,0,z)$ and $\mathbf{r}_{\mu}=(0.5a,0.5a,z)$, $\mathbf{r}=(100.5a,0.5a,z)$, for three different values of z, as indicated by the legends. All of the results are normalized to the amplitude of the corresponding Green tensor of vacuum.

parts of this quantity using black solid and dashed curves, as well as its envelope with a black shaded area. Analyzing the results of Figure 2, we notice that, in all cases, the real and imaginary parts of the Green tensor of the array display a fast oscillation similar to that of the Green tensor of vacuum, which arises from the factor $\exp(ik\Delta x)$ and, therefore, is a clear signature of their far-field character. Expectedly, this oscillation is not present in the envelope of the Green tensors. However, the Green tensor of the array stills displays a second, slower oscillation whose origin is more complex, as we explain later.

Another important characteristic of the results shown in Figure 2 is the significant change of the Green tensor of the array after the onset of the lattice resonance at the Γ point, which is indicated by the yellow dashed lines and coincides with those displayed in the insets of Figure 1b,c. Clearly, the contribution of the lattice resonance produces a very large enhancement of the amplitude of $G_{zz}^{EE}(\mathbf{r}, \mathbf{r}_{\mu})$, which grows as Δx increases. This enhancement is not as pronounced in the case of the yy component; indeed, for $\Delta x = 10a$, the Green tensor of the array is smaller than that of vacuum. The large difference between the yy and zz components is a direct consequence of the nature of the lattice resonances excited in each of these cases. For the yy component, the corresponding lattice resonance has an in-plane character in which the dipoles induced in the nanoparticles oscillate parallel to the array plane and therefore radiate very efficiently in the perpendicular direction. On the contrary, the lattice resonance corresponding to the zz component is an out-of-plane mode in which the dipoles oscillate perpendicular to the plane of the array. Consequently, they only radiate efficiently along the plane of the array, thus minimizing the radiative losses and producing the much larger values of the Green tensor shown in Figure 2. Indeed, out-of-plane lattice resonances have been investigated in the past for their large quality factors arising from the reduced radiative losses. $^{83-85}$

In all of the calculations shown in Figure 2, \mathbf{r}_{μ} and \mathbf{r} are separated along the x-axis. However, in Figure S2 of the Supporting Information, we analyze the amplitude of the Green tensor of the array for a similar displacement between \mathbf{r}_{μ} and \mathbf{r} , but, in this case, along the y-axis. As expected from the symmetry of the problem, $G_{zz}^{\mathrm{EE}}(\mathbf{r}, \mathbf{r}_{\mu})$ remains completely unchanged. However, the value for $G_{yy}^{\mathrm{EE}}(\mathbf{r}, \mathbf{r}_{\mu})$ becomes significantly smaller. The reason is that, in such a case, there is no lattice resonance involved, since they originate from the far-field coupling between the elements of the array, which vanishes along the direction parallel to the dipole moment induced in the nanoparticles.

The results displayed in Figure 2 demonstrate that $G_{zz}^{\rm EE}(\mathbf{r},\mathbf{r}_{\mu})$ is the dominant component of the Green tensor for the arrays under consideration. Therefore, in the following, we focus our analysis on this component. In Figure 3a, we plot the spectrum of $|G_{zz}^{\rm EE}(\mathbf{r},\mathbf{r}_{\mu})|/|G_{0,zz}^{\rm EE}(\mathbf{r}-\mathbf{r}_{\mu})|$ for $\mathbf{r}_{\mu}=(0,0,2R)$ and $\mathbf{r}=(\Delta x,0,2R)$, with $\Delta x=100a$ (red curve), 300a (black curve), and 600a (gray curve). As expected from the analysis above, once the lattice resonance begins to contribute (i.e., for $\lambda>832$ nm), it produces a very large enhancement of the amplitude of the Green tensor of the array. The enhancement increases with Δx , reaching a peak of \sim 90× the value of the Green tensor of vacuum for $\Delta x=600a$. In Figure 3a, as in the rest of the figures of this Article, we assume a=800 nm and R=100 nm.

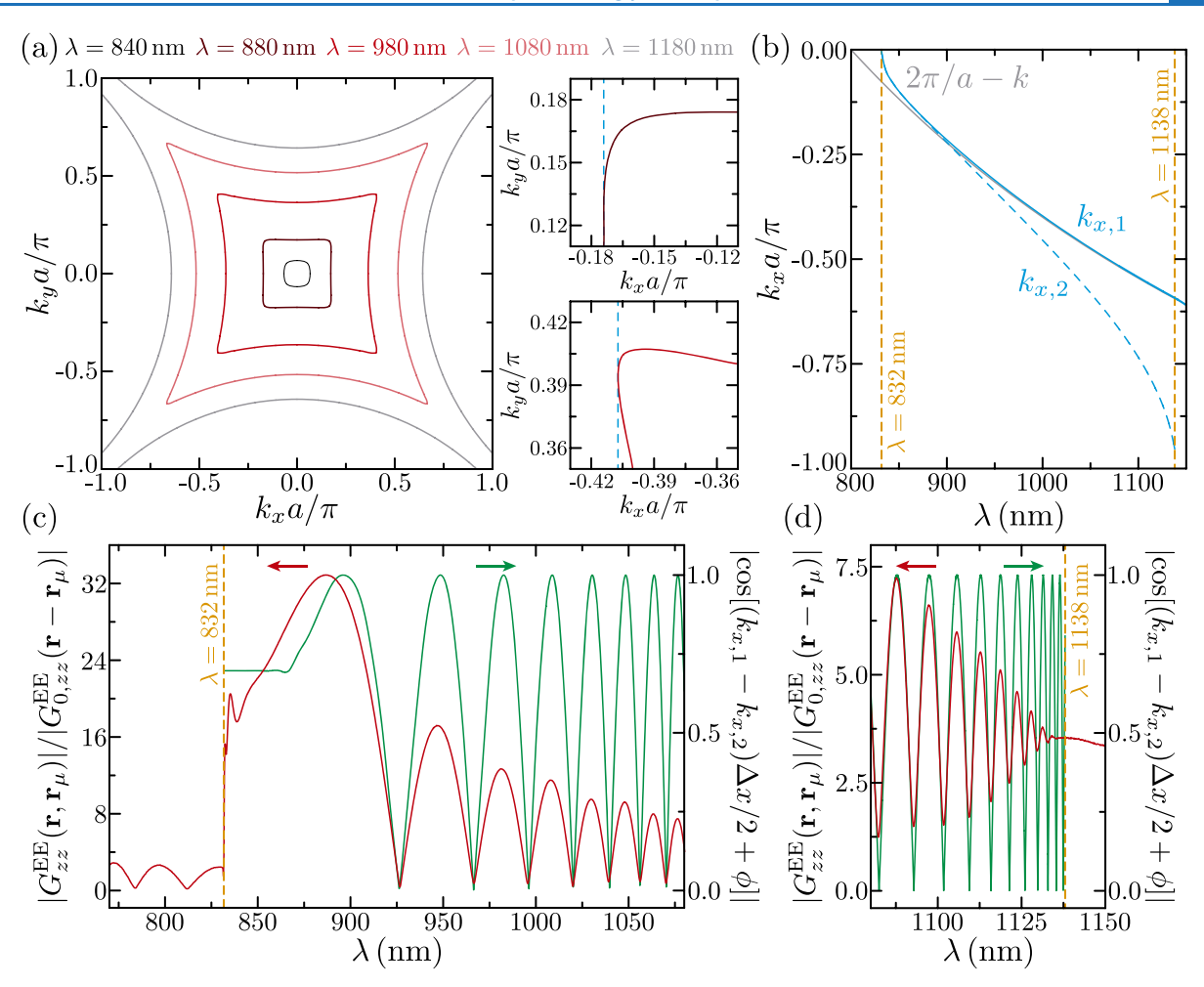


Figure 4. Analysis of the spectral characteristics of the Green tensor of a periodic array. (a) Iso-contours showing the position of the lattice resonance peak within the first Brillouin zone for different wavelengths. The panels on the right display a zoom of the iso-contours for $\lambda=880$ nm (upper panel) and $\lambda=980$ nm (lower panel). The blue dashed lines indicate $k_{x,2}$. (b) Value of $k_{x,1}$ (blue solid curve) and $k_{x,2}$ (blue dashed curve) as a function of wavelength. The gray curve represents the value of $2\pi/a - k$. (c, d) Normalized amplitude of the zz component of the Green tensor of the array connecting $\mathbf{r}_{\mu}=(0,0,2R)$ and $\mathbf{r}=(100a,0,2R)$ (red curves, left scales) and results of the analytical model of eq 5 (green curves, right scales). The yellow dashed lines in panels (b)–(d) mark the onset of the lattice resonance at the Γ point and its cutoff at the M point, as shown in the insets of Figure 1c. In all panels, we assume a=800 nm and R=100 nm.

However, it is important to understand how these results change when a and R are varied. To this end, in Figure S3 of the Supporting Information, we analyze the dependence of the Green tensor of the array on these parameters. In particular, we analyze arrays with a period of either a=700 or 800 nm, and a radius ranging from R=80 to 140 nm in steps of 20 nm. Examining these results, we observe a similar overall behavior in all of the cases analyzed. For a given a, however, the spectral position of the maximum value of the amplitude of the Green tensor shifts to larger wavelengths as R increases. This is consistent with the redshift of the lattice resonance onset for increasing R/a described in previous works. Furthermore, for each value of a, there is an optimum value of R that produces the largest enhancement of the Green tensor amplitude.

Another important aspect to analyze is the dependence of the Green tensor of the array on the position of \mathbf{r}_{μ} and \mathbf{r} within their respective unit cells. Figure 3b shows the spectrum of $|G_{zz}^{\mathrm{EE}}(\mathbf{r},\mathbf{r}_{\mu})|/|G_{0,zz}^{\mathrm{EE}}(\mathbf{r}-\mathbf{r}_{\mu})|$ for $\mathbf{r}_{\mu}=(x,y,2R)$ and $\mathbf{r}=(x+100a,y,2R)$ with the four different combinations of x and y depicted in the upper inset. The configuration in which both \mathbf{r}_{μ} and \mathbf{r} are located above a nanoparticle (red curve) results in the largest

values of the Green tensor, followed by the case in which both points lie at the center of the unit cell (green curve). The least favorable configurations correspond to \mathbf{r}_{μ} and \mathbf{r} located in between two of the nanoparticles, either along the x-axis (blue curve) or the y-axis (yellow curve). These results can be explained as a combination of two different factors: On one hand, the excitation of the lattice resonance, as well as the field that it produces, become stronger as \mathbf{r}_u and \mathbf{r} get closer to the nanoparticles, thus resulting in a larger value of the Green tensor. On the other hand, configurations in which \mathbf{r}_{μ} and \mathbf{r} are located in highly symmetrical points also favor a larger value of the Green tensor, since they minimize the cancelations due to phase differences in the excitation of the nanoparticles, as well as in the field that they produce. This last factor explains why the results for (x, y) = (0.5a, 0.5a) (green curve) are larger than those of (x, y) = (0.5a, 0) (blue curve) and (x, y) = (0, 0)0.5a) (yellow curve).

The value of the Green tensor also depends on the component of \mathbf{r}_{μ} and \mathbf{r} along the direction perpendicular to the array (i.e., the z-axis). We explore this dependence in Figures 3c and d, where we plot the spectrum of $|G_{zz}^{EE}(\mathbf{r}, \mathbf{r}_{\mu})|/|G_{0,zz}^{EE}(\mathbf{r} - \mathbf{r}_{\mu})|$ for $\mathbf{r}_{\mu} = (x, y, z)$ and $\mathbf{r} = (x + 100a, y, z)$ with

different values of z. Specifically, panels c and d show results for (x, y) = (0, 0) and (x, y) = (0.5a, 0.5a), respectively, with z ranging from 4R (lighter curves) to 1.5R (darker curves). Analyzing these results, we observe that, in both cases, the amplitude of the Green tensor grows as z decreases. However, while this growth accelerates for (x, y) = (0, 0) as \mathbf{r}_{μ} and \mathbf{r} approach the nanoparticles, it saturates for (x, y) = (0.5a, 0.5a).

Importantly, we have verified the accuracy of the dipole model by calculating the local density of states (LDOS)⁸⁶ induced by an individual metallic nanosphere, with the same characteristics as those of the arrays under consideration, and benchmarking it against full numerical solutions of Maxwell's equations. The results of this comparison are shown in Figure S4 of the Supporting Information. As we discussed above, a fully numerical calculation of the Green tensor of the array using a FEM or FDTD solver of Maxwell's equations is extremely challenging due to the lack of periodicity of the problem.

The spectra displayed in Figure 3 show that the onset of the contribution of the lattice resonance to the Green tensor is not influenced by \mathbf{r}_{μ} and \mathbf{r} . However, the oscillations of its amplitude are strongly dependent on Δx , but are not affected by the position of \mathbf{r}_{μ} and \mathbf{r} within their corresponding unit cells. In order to gain more insight into these behaviors, we start by invoking the following property of the lattice sum tensor: $\mathcal{G}(\mathbf{k}_{\parallel}, \mathbf{R}_i + \boldsymbol{\rho}) = \mathcal{G}(\mathbf{k}_{\parallel}, \boldsymbol{\rho})e^{i\mathbf{k}_{\parallel}\mathbf{R}_i}$, where \mathbf{R}_i is an arbitrary lattice vector. Using this relationship, we can rewrite eq 3 as

$$\mathbf{G}(\mathbf{r}, \mathbf{r}_{\mu}) = \frac{a^2}{4\pi^2} \int_{1BZ} d\mathbf{k}_{\parallel} e^{i\mathbf{k}_{\parallel}(\mathbf{R} - \mathbf{R}_{\mu})} \mathcal{G}(\mathbf{k}_{\parallel} \boldsymbol{\rho}) \mathcal{A}(\mathbf{k}_{\parallel}) \mathcal{G}(\mathbf{k}_{\parallel} \boldsymbol{-} \boldsymbol{\rho}_{\mu})$$

$$(4)$$

where we have defined $\rho={\bf r}-{\bf R}$ and $\rho_\mu={\bf r}_\mu-{\bf R}_{\mu\nu}$ with ${\bf R}$ and ${\bf R}_\mu$ being the lattice vectors corresponding to the unit cells in which ${\bf r}_\mu$ and ${\bf r}$ are located. From their definition, it is clear that the in-plane components of ρ and ρ_μ are located in the same unit cell. Therefore, eq 4 shows that the integral that defines the Green tensor of the array can be separated into two different factors: (i) an oscillating exponential that only depends on the separation between the unit cells in which ${\bf r}_\mu$ and ${\bf r}$ are located, and (ii) a term containing the response of the array, which only depends on the position of ${\bf r}_\mu$ and ${\bf r}$ within the unit cell.

As discussed in Figure 1, the response of the array is determined by the characteristics of its lattice resonances. Figure 4a shows the iso-contours indicating the position, within the first Brillouin zone, of the lowest-order lattice resonance of an array with a=800 nm and R=100 nm for the different values of the wavelength indicated by the labels. These iso-contours are obtained by finding the maximum value of $\mathcal{E}_{\hat{\mathbf{z}}}$ (see eq 2) and can be used to obtain an approximate expression for the Green tensor of the array. In particular, focusing again on the configuration with $\mathbf{r}_{\mu}=(0,0,2R)$ and $\mathbf{r}=(\Delta x,0,2R)$, and assuming that the response of the array is completely dominated by the lattice resonance, so that only the iso-contours contribute to the integral of eq 4, we can write

$$G_{zz}^{\text{EE}}(\mathbf{r}, \, \mathbf{r}_{\mu}) \sim e^{ik_{x,1}\Delta x} + e^{ik_{x,2}\Delta x}e^{-i2\phi}$$

$$= 2e^{i(k_{x,1}+k_{x,2})\Delta x/2}e^{-i\phi} \cos[(k_{x,1}-k_{x,2})\Delta x/2 + \phi]$$
(5)

Here, ϕ is a constant phase, while $k_{x,1}$ and $k_{x,2}$ represent, in the spirit of the stationary phase approximation, the points of the

lattice resonance iso-contours that have a zero derivative with respect to k_v . These are the only points that contribute to the integral, since the rapid oscillation of the exponential factor cancels the contribution of the rest of the iso-contour. The first of these points, $k_{x,1}$, corresponds to the value of k_x at which the iso-contour intercepts the k_x -axis. The other one, $k_{x,2}$, as shown by the blue dashed lines in the right panels of Figure 4a, is located near the corners of the iso-contour. Figure 4b shows the value of $k_{x,1}$ and $k_{x,2}$ as a function of wavelength. As expected from the shape of the iso-contours, $k_{x,1}$ and $k_{x,2}$ take identical values for wavelengths near the onset of the lattice resonance at the Γ point (i.e., λ = 832 nm). However, as λ grows, their values become increasingly different. Importantly, the value of $k_{x,2}$ saturates as the wavelength approaches the cutoff of the lattice resonance at the M point (i.e., $\lambda = 1138$ nm). These limits at the Γ and M points are indicated with yellow dashed lines in Figure 4b, as well as in the insets of Figure 1c. It is important to mention that, in our analysis, we only consider the $k_{x,1}$ and $k_{x,2}$ located in the negative part of the k_x -axis. The reason is that the lowest order lattice resonance has a negative group velocity, as can be seen in Figure 1c, and therefore, only the components with negative k_x contribute to the Green tensor connecting the points $\mathbf{r}_{\mu} = (0, 0, 2R)$ and $\mathbf{r} =$ $(\Delta x, 0, 2R)$ for positive values of Δx . This is confirmed numerically in Figure S5 of the Supporting Information.

The analytical approximation given in eq 5 predicts two different oscillatory behaviors. First, the exponential factor oscillates as the value of $(k_{x,1} + k_{x,2})\Delta x/2$ changes with wavelength. Since, as can be inferred from Figure 4b, the value of $(k_{x,1} + k_{x,2})/2$ is very similar to $2\pi/a - k$ (solid gray curve), especially for wavelengths below ~1050 nm, this factor explains the fast oscillation of the real and imaginary parts of $\mathbf{G}^{\mathrm{EE}}(\mathbf{r}, \mathbf{r}_{\mu})$ observed in Figure 2. Second, the cosine factor produces a slower oscillation determined by the change of $(k_{x,1})$ $-k_{x,2}\Delta x/2$ with λ . As we analyze in Figure 4c, this oscillation reproduces that of the amplitude of the Green tensor of the array discussed in Figures 2 and 3. In particular, the green curve (right scale) displays the value of $lcos[(k_{x,1} - k_{x,2})\Delta x/2]$ $+\phi$], with $k_{x,1}$ and $k_{x,2}$ taken from panel b, $\Delta x=100a$, and $\phi=$ 0.8, while the red curve (left scale) shows $|G_{zz}^{\text{EE}}(\mathbf{r}, \mathbf{r}_{\mu})|/|G_{0,zz}^{\text{EE}}(\mathbf{r}, \mathbf{r}_{\mu})|$ $-\mathbf{r}_{u}$). Comparing these two curves, we observe that the cosine factor of eq 5 perfectly matches the oscillations of the amplitude of the Green tensor above the onset of the lattice resonance (i.e., $\lambda = 832$ nm). Furthermore, since $k_{x,2}$ saturates at $\lambda = 1138$ nm, it is expected that these oscillations disappear beyond that cutoff. This prediction is confirmed by the results plotted in Figure 4d, which extend those of panel c to the wavelength range around 1138 nm. Clearly, the oscillations of the amplitude of the Green tensor vanish as the wavelength approaches the cutoff indicated by the yellow dashed line, a behavior that is perfectly captured by the analytical approximation.

Then, from the results discussed in Figure 4 and the analytical approximation of eq 5, we conclude that the contribution of the lowest-order lattice resonance to the Green tensor of the array occurs through a combination of parallel wavevectors. One of them is always pointing along the direction connecting ${\bf r}$ with ${\bf r}_\mu$, while the value of the other varies with the wavelength. When the wavevectors are equal, as is the case for $\lambda \sim 880$ nm, the amplitude of the Green tensor reaches its maximum value. However, as they become different, their contributions interfere, resulting in the oscillation of the amplitude of the Green tensor. Although these conclusions

arise from the analysis of a particular set of \mathbf{r}_{μ} and \mathbf{r} , they can be readily extended to other configurations using symmetry arguments.

In order to complete our characterization of the Green tensor of the array, we analyze, in Figure 5a, its dependence

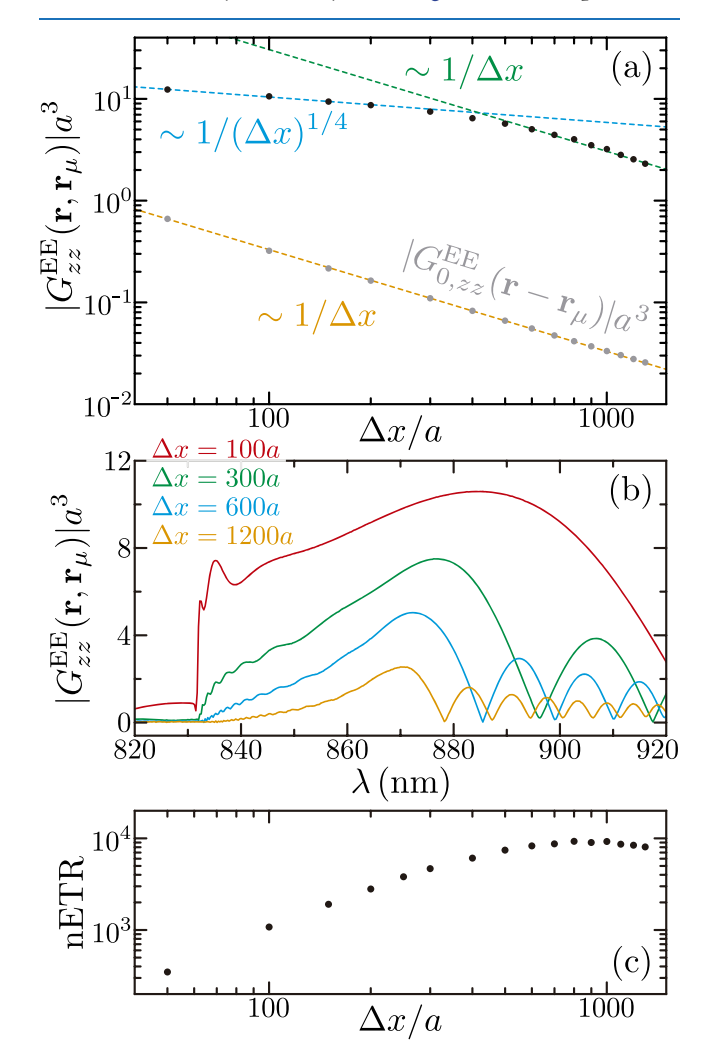


Figure 5. Analysis of the dependence with $|\mathbf{r} - \mathbf{r}_{\mu}|$ of the Green tensor of a periodic array with a=800 nm and R=100 nm. The black dots in panel (a) show $|G_{zz}^{\rm EE}(\mathbf{r},\mathbf{r}_{\mu})|$, for $\mathbf{r}_{\mu}=(0,0,2R)$ and $\mathbf{r}=(\Delta x,0,2R)$ as a function of Δx . For each Δx , we calculate $|G_{zz}^{\rm EE}(\mathbf{r},\mathbf{r}_{\mu})|$ at the wavelength that produces the largest value. For comparison, the gray dots represent $|G_{0,zz}^{\rm EE}(\mathbf{r} - \mathbf{r}_{\mu})|$, evaluated at the same positions and wavelengths. The dashed lines mark different scaling functions as indicated by the corresponding labels. (b) Spectrum of $|G_{zz}^{\rm EE}(\mathbf{r},\mathbf{r}_{\mu})|$ for the different values of Δx shown in the legend. (c) Normalized energy transfer rate calculated from the data shown in panel (a) as nETR = $|G_{zz}^{\rm EE}(\mathbf{r},\mathbf{r}_{\mu})|^2/|G_{0,zz}^{\rm EE}(\mathbf{r}-\mathbf{r}_{\mu})|^2$.

with the distance between \mathbf{r}_{μ} and \mathbf{r} . Specifically, we consider an array with a=800 nm and R=100 nm, and take $\mathbf{r}_{\mu}=(0,0,2R)$ and $\mathbf{r}=(\Delta x,0,2R)$. We use black dots to plot the value of $|G_{zz}^{\mathrm{EE}}(\mathbf{r},\mathbf{r}_{\mu})|$ as a function of Δx . For each value of Δx , we evaluate $|G_{zz}^{\mathrm{EE}}(\mathbf{r},\mathbf{r}_{\mu})|$ at the wavelength for which it reaches its maximum value. As a reference, we also plot, using gray dots, the value of the amplitude of the Green tensor of vacuum $|G_{0,zz}^{\mathrm{EE}}(\mathbf{r}-\mathbf{r}_{\mu})|$, evaluated at the same positions and wavelengths. Analyzing these results, we observe that, while the Green tensor of vacuum always decays as $(\Delta x)^{-1}$, as expected from the far-field character of the distances under consid-

eration, $|G_{zz}^{\rm EE}({\bf r},{\bf r}_\mu)|$ displays two distinct behaviors. For $\Delta x\lesssim 400a$, it decays at a much slower rate, following an approximate dependence of $\sim (\Delta x)^{-1/4}$. However, for $\Delta x\gtrsim 400a$, the decay accelerates to $\sim (\Delta x)^{-1}$, similar to that of the Green tensor of vacuum. This change of behavior can be understood by looking at the spectra of $|G_{zz}^{\rm EE}({\bf r},{\bf r}_\mu)|$ plotted in Figure 5b. There we see how, as Δx increases, the first minimum caused by the oscillations of the Green tensor shifts toward smaller wavelengths. For $\Delta x\gtrsim 400a$, this minimum reaches the wavelengths at which the amplitude of the Green tensor achieves its maximum value ($\lambda\sim 880$ nm) and forces it to decrease, thus, producing the faster decay rate observed in panel a.

The results shown in panel a demonstrate that the contribution of the lattice resonance produces a large enhancement of the Green tensor of the array as compared with its vacuum counterpart. This enhancement can mediate the transfer of energy between dipole emitters placed in the vicinity of the array. In order to quantify this effect, we plot, in Figure 5c, the normalized energy transfer rate, defined as ^{87,88}

nETR =
$$\frac{|G_{zz}^{EE}(\mathbf{r}, \mathbf{r}_{\mu})|^2}{|G_{0,z}^{EE}(\mathbf{r} - \mathbf{r}_{\mu})|^2}$$

This quantity measures the enhancement of the energy transfer between two electric dipole emitters located at \mathbf{r}_{μ} and \mathbf{r} provided by the array. We assume that both dipoles are oriented along the z-axis since, as discussed before, that is the optimum configuration to maximize the contribution of the array. The results shown in Figure 5c clearly demonstrate that, thanks to the contribution of the lattice resonance, the array under investigation produces a nETR with values in the range of 10³ to 10⁴ for distances of hundreds to thousands of periods. These distances are completely consistent with an estimation of the propagation length of the lattice resonance L, which can be obtained from the inverse of its fwhm extracted from the results of Figure 1c for a fixed value of λ (i.e., from a horizontal cut). By doing so, for a wavelength of $\lambda = 880$ nm, we obtain L ~ 700a. All of these results confirm that periodic arrays of metallic nanostructures are capable of enhancing the longrange coupling between dipole emitters.

CONCLUSIONS

In summary, we have performed a detailed investigation of the coupling between dipole emitters mediated by the lattice resonances of a periodic array of metallic nanoparticles. To do so, we have derived a closed expression for the Green tensor of the array using a rigorous coupled dipole model and used it to analyze its spectral and spatial characteristics. We have focused on the electric-electric term of the Green tensor, which represents the electric field produced by the array when excited by a unit electric dipole, and analyzed both its yy and the zz components. By doing so, we have found that the latter reaches much larger values due to the contribution of the out-of-plane lattice resonance, which displays much lower radiative losses than its in-plane counterpart. Through the analysis of the spectrum of the Green tensor connecting different pairs of points r, and r, we have found that, in addition to a fast oscillation of its real and imaginary parts arising from its farfield nature, the amplitude of the Green tensor displays a slower oscillation. This oscillation depends on $|\mathbf{r} - \mathbf{r}_u|$, but not on the position of these points within the unit cells in which they are located. We have explained this behavior as the result

of an interference process produced by the excitation of a lattice resonance with different parallel wavevectors. By comparing the Green tensor of the array with its vacuum counterpart, we have found that the contribution of the lattice resonance results in extraordinarily large values that decay with $|\mathbf{r} - \mathbf{r}_{\mu}|$ at a much slower rate. This demonstrates that the lattice resonances of periodic arrays of metallic nanoparticles can mediate an efficient long-range coupling between dipole emitters placed in their vicinity. Although, in this Article, we have focused on arrays of metallic nanoparticles, our theoretical approach is also valid for investigating other systems, such as arrays of dielectric nanostructures. 89 Furthermore, our analysis can be readily applied to periodic arrays of atoms by using the appropriate polarizability. 90-94 The results of this Article expand the fundamental knowledge of lattice resonances and pave the way for the use of periodic arrays of metallic nanostructures as platforms to enhance the long-range coupling between dipole emitters.

METHODS

Derivation of the Polarizability of the Array. As stated in the main text, we use a coupled dipole model^{1,3,19,75,77} and describe each of the nanoparticles of the array as a point dipole with both electric **p** and magnetic **m** components. The dipole induced in the nanoparticle of the array located at \mathbf{R}_p when excited by an external electromagnetic field with electric and magnetic amplitudes \mathbf{E}_i and \mathbf{B}_p respectively, can be written as

$$\begin{bmatrix} \mathbf{P}_i \\ \mathbf{m}_i \end{bmatrix} = \begin{bmatrix} \boldsymbol{\alpha}^{\mathrm{E}} & \mathbf{0} \\ \mathbf{0} & \boldsymbol{\alpha}^{\mathrm{M}} \end{bmatrix} \begin{bmatrix} \mathbf{E}_i \\ \mathbf{B}_i \end{bmatrix} + \sum_{j \neq i} \begin{bmatrix} \mathbf{G}_0^{\mathrm{EE}}(\mathbf{R}_i - \mathbf{R}_j) & \mathbf{G}_0^{\mathrm{EM}}(\mathbf{R}_i - \mathbf{R}_j) \\ \mathbf{G}_0^{\mathrm{ME}}(\mathbf{R}_i - \mathbf{R}_j) & \mathbf{G}_0^{\mathrm{MM}}(\mathbf{R}_i - \mathbf{R}_j) \end{bmatrix} \begin{bmatrix} \mathbf{p}_j \\ \mathbf{m}_j \end{bmatrix}$$

Here, $\pmb{\alpha}^{\rm E}$ and $\pmb{\alpha}^{\rm M}$ are the electric and magnetic polarizability tensors of the nanoparticles, while $\mathbf{G}_0^{\rm EE}(\mathbf{r}) = \mathbf{G}_0^{\rm MM}(\mathbf{r}) = [k^2 I_{3\times3} + \nabla \nabla] e^{\mathrm{i}k|\mathbf{r}|}/|\mathbf{r}|$ and $\mathbf{G}_0^{\rm EM}(\mathbf{r}) = -\mathbf{G}_0^{\rm ME}(\mathbf{r}) = ik\nabla \times e^{ik|\mathbf{r}|}/|\mathbf{r}|$ represent the different components of the Green tensor of vacuum, with $k=2\pi/\lambda$ being the wavenumber of light (notice that we use Gaussian units). Taking advantage of the periodicity of the array and using the Fourier transform defined as $v_i = \frac{a^2}{4\pi^2} \int_{\rm 1BZ} d\mathbf{k}_{\parallel} \, \nu(\mathbf{k}_{\parallel}) e^{i\mathbf{k}_{\parallel} \cdot \mathbf{R}_i}$, where a is the array period and 1BZ stands for the first Brillouin zone, we can write the following self-consistent equation for the \mathbf{k}_{\parallel} components of the dipole induced in the nanoparticles

$$\begin{bmatrix} \mathbf{p}(\mathbf{k}_{\parallel}) \\ \mathbf{m}(\mathbf{k}_{\parallel}) \end{bmatrix} = \begin{bmatrix} \boldsymbol{\alpha}^{E} & 0 \\ 0 & \boldsymbol{\alpha}^{M} \end{bmatrix} \begin{bmatrix} \mathbf{E}(\mathbf{k}_{\parallel}) \\ \mathbf{B}(\mathbf{k}_{\parallel}) \end{bmatrix} + \begin{bmatrix} \mathcal{G}^{EE}(\mathbf{k}_{\parallel} & 0) & \mathcal{G}^{EM}(\mathbf{k}_{\parallel} & 0) \\ -\mathcal{G}^{EM}(\mathbf{k}_{\parallel} & 0) & \mathcal{G}^{EE}(\mathbf{k}_{\parallel} & 0) \end{bmatrix} \begin{bmatrix} \mathbf{p}(\mathbf{k}_{\parallel}) \\ \mathbf{m}(\mathbf{k}_{\parallel}) \end{bmatrix}$$
(6)

In this expression, $G^{\nu}(\mathbf{k}_{\parallel}, \mathbf{r}) = \sum_{i}^{'} \mathbf{G}_{0}^{\nu}(\mathbf{R}_{i} + \mathbf{r})e^{-i\mathbf{k}_{\parallel}\mathbf{R}_{i}}$ with $\nu =$ EE, EM and the prime in the summation indicates that, if a term satisfies $\mathbf{R}_{i} + \mathbf{r} = 0$, it is to be excluded. Equation 6 can be solved as

$$\begin{bmatrix} \mathbf{p}(\mathbf{k}_{\parallel}) \\ \mathbf{m}(\mathbf{k}_{\parallel}) \end{bmatrix} = \mathcal{A}(\mathbf{k}_{\parallel}) \begin{bmatrix} \mathbf{E}(\mathbf{k}_{\parallel}) \\ \mathbf{B}(\mathbf{k}_{\parallel}) \end{bmatrix}$$
(7)

where

$$\mathcal{A}(\mathbf{k}_{\parallel}) = \left[\begin{bmatrix} \boldsymbol{\alpha}^{\mathrm{E}} & 0 \\ 0 & \boldsymbol{\alpha}^{\mathrm{M}} \end{bmatrix}^{-1} - \begin{bmatrix} \mathcal{G}^{\mathrm{EE}}(\mathbf{k}_{\parallel} & 0) & \mathcal{G}^{\mathrm{EM}}(\mathbf{k}_{\parallel} & 0) \\ -\mathcal{G}^{\mathrm{EM}}(\mathbf{k}_{\parallel} & 0) & \mathcal{G}^{\mathrm{EE}}(\mathbf{k}_{\parallel} & 0) \end{bmatrix} \right]^{-1}$$
(8)

is the polarizability of the array.

Derivation of the \mathbf{k}_{\parallel} Components of the Electromagnetic Field of a Point Dipole. Given a unit dipole with electric $\hat{\boldsymbol{\mu}}^{\mathrm{E}}$ and magnetic $\hat{\boldsymbol{\mu}}^{\mathrm{M}}$ components, oscillating at frequency $\boldsymbol{\omega}$ and located at \mathbf{r}_{μ} we can use the array scanning method 76,95 to write its associated current as

$$\begin{bmatrix} \mathbf{j}^{\mathrm{E}}(\mathbf{r}) \\ \mathbf{j}^{\mathrm{M}}(\mathbf{r}) \end{bmatrix} = \frac{a^{2}}{4\pi^{2}} \int_{1BZ} d\mathbf{k}_{\parallel} (-i\omega) \sum_{i} \delta(\mathbf{r} - \mathbf{r}_{\mu} + \mathbf{R}_{i}) e^{-i\mathbf{k}_{\parallel} \mathbf{R}_{i}} \begin{bmatrix} \hat{\boldsymbol{\mu}}^{\mathrm{E}} \\ \hat{\boldsymbol{\mu}}^{\mathrm{M}} \end{bmatrix}$$
(9)

Then, taking into account that the electromagnetic field produced by the dipole current at the position of one of the nanoparticles of the array can be written as

$$\begin{bmatrix} \mathbf{E}_i \\ \mathbf{B}_i \end{bmatrix} = \frac{i}{\omega} \int d\mathbf{r}' \begin{bmatrix} \mathbf{G}_0^{\mathrm{EE}}(\mathbf{R}_i - \mathbf{r}') & \mathbf{G}_0^{\mathrm{EM}}(\mathbf{R}_i - \mathbf{r}') \\ -\mathbf{G}_0^{\mathrm{EM}}(\mathbf{R}_i - \mathbf{r}') & \mathbf{G}_0^{\mathrm{EE}}(\mathbf{R}_i - \mathbf{r}') \end{bmatrix} \begin{bmatrix} \mathbf{j}^{\mathrm{E}}(\mathbf{r}') \\ \mathbf{j}^{\mathrm{M}}(\mathbf{r}') \end{bmatrix}$$

and using eq 9, we obtain

$$\begin{bmatrix} \mathbf{E}(\mathbf{k}_{\parallel}) \\ \mathbf{B}(\mathbf{k}_{\parallel}) \end{bmatrix} = \begin{bmatrix} \mathcal{G}^{\mathrm{EE}}(\mathbf{k}_{\parallel}, -\mathbf{r}_{\mu}) & \mathcal{G}^{\mathrm{EM}}(\mathbf{k}_{\parallel}, -\mathbf{r}_{\mu}) \\ -\mathcal{G}^{\mathrm{EM}}(\mathbf{k}_{\parallel}, -\mathbf{r}_{\mu}) & \mathcal{G}^{\mathrm{EE}}(\mathbf{k}_{\parallel}, -\mathbf{r}_{\mu}) \end{bmatrix} \begin{bmatrix} \hat{\boldsymbol{\mu}}^{\mathrm{E}} \\ \hat{\boldsymbol{\mu}}^{\mathrm{M}} \end{bmatrix}$$
(10)

Derivation of the Electromagnetic Field Produced by a Periodic Array of Dipoles. We can write the electromagnetic field produced at a point **r** outside of the array by a periodic array of dipoles as

$$\begin{bmatrix} \mathbf{E}(\mathbf{r}) \\ \mathbf{B}(\mathbf{r}) \end{bmatrix} = \sum_{i} \begin{bmatrix} \mathbf{G}_{0}^{\text{EE}}(\mathbf{r} - \mathbf{R}_{i}) & \mathbf{G}_{0}^{\text{EM}}(\mathbf{r} - \mathbf{R}_{i}) \\ -\mathbf{G}_{0}^{\text{EM}}(\mathbf{r} - \mathbf{R}_{i}) & \mathbf{G}_{0}^{\text{EE}}(\mathbf{r} - \mathbf{R}_{i}) \end{bmatrix} \begin{bmatrix} \mathbf{p}_{i} \\ \mathbf{m}_{i} \end{bmatrix}$$

Then, expressing the dipoles in terms of their k_{\parallel} components, we have

$$\begin{bmatrix} \mathbf{E}(\mathbf{r}) \\ \mathbf{B}(\mathbf{r}) \end{bmatrix} = \frac{a^2}{4\pi^2} \int_{1BZ} d\mathbf{k}_{\parallel} \begin{bmatrix} \mathcal{G}^{EE}(\mathbf{k}_{\parallel}, \mathbf{r}) & \mathcal{G}^{EM}(\mathbf{k}_{\parallel}, \mathbf{r}) \\ -\mathcal{G}^{EM}(\mathbf{k}_{\parallel}, \mathbf{r}) & \mathcal{G}^{EE}(\mathbf{k}_{\parallel}, \mathbf{r}) \end{bmatrix} \begin{bmatrix} \mathbf{p}(\mathbf{k}_{\parallel}) \\ \mathbf{m}(\mathbf{k}_{\parallel}) \end{bmatrix}$$

Finally, substituting eqs 7 and 10 into the expression above, we obtain eq 1.

ASSOCIATED CONTENT

Supporting Information

The Supporting Information is available free of charge at https://pubs.acs.org/doi/10.1021/acsphotonics.1c01463.

Different benchmarks of the dipole model; analysis of the Green tensor of the array for different combinations of \mathbf{r}_{μ} , \mathbf{r} , a, and R; analysis of the contribution of the positive and negative \mathbf{k}_{\parallel} components of the Green tensor of the array (PDF)

AUTHOR INFORMATION

Corresponding Author

Alejandro Manjavacas — Department of Physics and Astronomy, University of New Mexico, Albuquerque, New Mexico 87106, United States; Instituto de Óptica (IO-CSIC), Consejo Superior de Investigaciones Científicas, 28006 Madrid, Spain; orcid.org/0000-0002-2379-1242; Email: a.manjavacas@csic.es

Authors

Lauren Zundel – Department of Physics and Astronomy, University of New Mexico, Albuquerque, New Mexico 87106, United States; orcid.org/0000-0003-1850-5210

- Alvaro Cuartero-González Departamento de Física Teórica de la Materia Condensada and Condensed Matter Physics Center (IFIMAC), Universidad Autónoma de Madrid, E-28049 Madrid, Spain; Mechanical Engineering Department, ICAI, Universidad Pontificia Comillas, 28015 Madrid, Spain
- Stephen Sanders Department of Physics and Astronomy, University of New Mexico, Albuquerque, New Mexico 87106, United States
- Antonio I. Fernández-Domínguez Departamento de Física Teórica de la Materia Condensada and Condensed Matter Physics Center (IFIMAC), Universidad Autónoma de Madrid, E-28049 Madrid, Spain; orcid.org/0000-0002-8082-395X

Complete contact information is available at: https://pubs.acs.org/10.1021/acsphotonics.1c01463

Funding

Spanish MCIN, U.S. National Science Foundation, and U.S. Department of Energy.

Notes

The authors declare no competing financial interest.

ACKNOWLEDGMENTS

This work has been sponsored by Grant Nos. TEM-FLU PID2019-109502GA-I00, MDM-2014-0377-16-4, and RTI2018-099737-BI00 funded by MCIN/AEI/10.13039/501100011033 and by "ERDF A way of making Europe," as well as the U.S. National Science Foundation (Grant No. DMR-1941680). L.Z. acknowledges support from the Department of Energy Computational Science Graduate Fellowship (Grant No. DE-SC0020347). We would also like to thank the UNM Center for Advanced Research Computing, supported in part by the U.S. National Science Foundation, for providing some of the computational resources used in this work.

REFERENCES

- (1) Zhao, L.; Kelly, K. L.; Schatz, G. C. The extinction spectra of silver nanoparticle arrays: influence of array structure on plasmon resonance wavelength and width. *J. Phys. Chem. B* **2003**, *107*, 7343–7350.
- (2) Zou, S.; Janel, N.; Schatz, G. C. Silver nanoparticle array structures that produce remarkably narrow plasmon lineshapes. *J. Chem. Phys.* **2004**, *120*, 10871–10875.
- (3) García de Abajo, F. J. Colloquium: Light scattering by particle and hole arrays. *Rev. Mod. Phys.* **2007**, *79*, 1267–1290.
- (4) Auguié, B.; Barnes, W. L. Collective resonances in gold nanoparticle Arrays. *Phys. Rev. Lett.* **2008**, *101*, 143902.
- (5) Kravets, V. G.; Schedin, F.; Grigorenko, A. N. Extremely narrow plasmon resonances based on diffraction coupling of localized plasmons in arrays of metallic nanoparticles. *Phys. Rev. Lett.* **2008**, *101*, 087403.
- (6) Chu, Y.; Schonbrun, E.; Yang, T.; Crozier, K. B. Experimental observation of narrow surface plasmon resonances in gold nanoparticle arrays. *Appl. Phys. Lett.* **2008**, *93*, 181108.
- (7) Vecchi, G.; Giannini, V.; Gómez Rivas, J. Surface modes in plasmonic crystals induced by diffractive coupling of nanoantennas. *Phys. Rev. B* **2009**, *80*, 201401.
- (8) Vitrey, A.; Aigouy, L.; Prieto, P.; García-Martín, J. M.; González, M. U. Parallel Collective Resonances in Arrays of Gold Nanorods. *Nano Lett.* **2014**, *14*, 2079–2085.
- (9) Humphrey, A. D.; Meinzer, N.; Starkey, T. A.; Barnes, W. L. Surface Lattice Resonances in Plasmonic Arrays of Asymmetric Disc Dimers. *ACS Photonics* **2016**, *3*, 634–639.

- (10) Humphrey, A. D.; Barnes, W. L. Plasmonic surface lattice resonances in arrays of metallic nanoparticle dimers. *J. Opt.* **2016**, *18*, 035005.
- (11) Wang, W.; Ramezani, M.; Väkeväinen, A. I.; Törmä, P.; Gómez Rivas, J.; Odom, T. W. The rich photonic world of plasmonic nanoparticle arrays. *Mater. Today* **2018**, *21*, 303–314.
- (12) Kravets, V. G.; Kabashin, A. V.; Barnes, W. L.; Grigorenko, A. N. Plasmonic Surface Lattice Resonances: A Review of Properties and Applications. *Chem. Rev.* **2018**, *118*, 5912–5951.
- (13) Cherqui, C.; Bourgeois, M. R.; Wang, D.; Schatz, G. C. Plasmonic Surface Lattice Resonances: Theory and Computation. *Acc. Chem. Res.* **2019**, *52*, 2548–2558.
- (14) Juodėnas, M.; Tamulevičius, T.; Henzie, J.; Erts, D.; Tamulevičius, S. Surface Lattice Resonances in Self-Assembled Arrays of Monodisperse Ag Cuboctahedra. ACS Nano 2019, 13, 9038–9047.
- (15) Utyushev, A. D.; Zakomirnyi, V. I.; Rasskazov, I. L. Collective lattice resonances: Plasmonics and beyond. *Rev. Phys.* **2021**, *6*, 100051.
- (16) Adato, R.; Yanik, A. A.; Wu, C.-H.; Shvets, G.; Altug, H. Radiative engineering of plasmon lifetimes in embedded nanoantenna arrays. *Opt. Express* **2010**, *18*, 4526–4537.
- (17) Zakomirnyi, V. I.; Rasskazov, I. L.; Gerasimov, V. S.; Ershov, A. E.; Polyutov, S. P.; Karpov, S. V. Refractory titanium nitride twodimensional structures with extremely narrow surface lattice resonances at telecommunication wavelengths. *Appl. Phys. Lett.* **2017**, *111*, 123107.
- (18) Khlopin, D.; Laux, F.; Wardley, W. P.; Martin, J.; Wurtz, G. A.; Plain, J.; Bonod, N.; Zayats, A. V.; Dickson, W.; Gérard, D. Lattice modes and plasmonic linewidth engineering in gold and aluminum nanoparticle arrays. *J. Opt. Soc. Am. B* **2017**, *34*, 691–700.
- (19) Baur, S.; Sanders, S.; Manjavacas, A. Hybridization of Lattice Resonances. ACS Nano 2018, 12, 1618–1629.
- (20) Le-Van, Q.; Zoethout, E.; Geluk, E.-J.; Ramezani, M.; Berghuis, M.; Gómez Rivas, J. Enhanced Quality Factors of Surface Lattice Resonances in Plasmonic Arrays of Nanoparticles. *Adv. Opt. Mater.* **2019**, *7*, 1801451.
- (21) Zhu, X.; Imran Hossain, G. M.; George, M.; Farhang, A.; Cicek, A.; Yanik, A. A. Beyond Noble Metals: High Q-Factor Aluminum Nanoplasmonics. *ACS Photonics* **2020**, *7*, 416–424.
- (22) Deng, S.; Li, R.; Park, J.-E.; Guan, J.; Choo, P.; Hu, J.; Smeets, P. J. M.; Odom, T. W. Ultranarrow plasmon resonances from annealed nanoparticle lattices. *Proc. Natl. Acad. Sci. U. S. A.* **2020**, *117*, 23380–23384.
- (23) Cuartero-González, A.; Sanders, S.; Zundel, L.; Fernández-Domínguez, A. I.; Manjavacas, A. Super- and Subradiant Lattice Resonances in Bipartite Nanoparticle Arrays. *ACS Nano* **2020**, *14*, 11876
- (24) Bin-Alam, M. S.; Reshef, O.; Mamchur, Y.; Alam, M. Z.; Carlow, G.; Upham, J.; Sullivan, B. T.; Ménard, J.-M.; Huttunen, M. J.; Boyd, R. W.; Dolgaleva, K. Ultra-high-Q resonances in plasmonic metasurfaces. *Nat. Commun.* **2021**, *12*, 974.
- (25) Zundel, L.; May, A.; Manjavacas, A. Lattice Resonances Induced by Periodic Vacancies in Arrays of Nanoparticles. *ACS Photonics* **2021**, *8*, 360–368.
- (26) Adato, R.; Yanik, A. A.; Amsden, J. J.; Kaplan, D. L.; Omenetto, F. G.; Hong, M. K.; Erramilli, S.; Altug, H. Ultra-sensitive vibrational spectroscopy of protein monolayers with plasmonic nanoantenna arrays. *Proc. Natl. Acad. Sci. U. S. A.* 2009, 106, 19227–19232.
- (27) Thackray, B. D.; Kravets, V. G.; Schedin, F.; Auton, G.; Thomas, P. A.; Grigorenko, A. N. Narrow Collective Plasmon Resonances in Nanostructure Arrays Observed at Normal Light Incidence for Simplified Sensing in Asymmetric Air and Water Environments. ACS Photonics 2014, 1, 1116–1126.
- (28) Danilov, A.; Tselikov, G.; Wu, F.; Kravets, V. G.; Ozerov, I.; Bedu, F.; Grigorenko, A. N.; Kabashin, A. V. Ultra-narrow surface lattice resonances in plasmonic metamaterial arrays for biosensing applications. *Biosens. Bioelectron.* **2018**, *104*, 102–112.
- (29) Matricardi, C.; Hanske, C.; Garcia-Pomar, J. L.; Langer, J.; Mihi, A.; Liz-Marzán, L. M. Gold Nanoparticle Plasmonic Super-

- lattices as Surface-Enhanced Raman Spectroscopy Substrates. ACS Nano 2018, 12, 8531-8539.
- (30) Väkeväinen, A. I.; Moerland, R. J.; Rekola, H. T.; Eskelinen, A.-P.; Martikainen, J.-P.; Kim, D.-H.; Törmä, P. Plasmonic Surface Lattice Resonances at the Strong Coupling Regime. *Nano Lett.* **2014**, 14, 1721–1727.
- (31) Todisco, F.; Esposito, M.; Panaro, S.; De Giorgi, M.; Dominici, L.; Ballarini, D.; Fernández-Domínguez, A. I.; Tasco, V.; Cuscunà, M.; Passaseo, A.; Ciracì, C.; Gigli, G.; Sanvitto, D. Toward Cavity Quantum Electrodynamics with Hybrid Photon Gap-Plasmon States. *ACS Nano* **2016**, *10*, 11360–11368.
- (32) Rodriguez, S. R. K.; Feist, J.; Verschuuren, M. A.; Garcia Vidal, F. J.; Gómez Rivas, J. Thermalization and Cooling of Plasmon-Exciton Polaritons: Towards Quantum Condensation. *Phys. Rev. Lett.* **2013**, *111*, 166802.
- (33) Ramezani, M.; Halpin, A.; Fernández-Domínguez, A. I.; Feist, J.; Rodriguez, S. R.-K.; Garcia-Vidal, F. J.; Gómez Rivas, J. Plasmon-exciton-polariton lasing. *Optica* **2017**, *4*, 31–37.
- (34) Hakala, T. K.; Moilanen, A. J.; Väkeväinen, A. I.; Guo, R.; Martikainen, J.-P.; Daskalakis, K. S.; Rekola, H. T.; Julku, A.; Törmä, P. Bose–Einstein condensation in a plasmonic lattice. *Nat. Phys.* **2018**, *14*, 739–744.
- (35) Rodriguez, S. R. K.; Lozano, G.; Verschuuren, M. A.; Gomes, R.; Lambert, K.; De Geyter, B.; Hassinen, A.; Van Thourhout, D.; Hens, Z.; Gomez Rivas, J. Quantum rod emission coupled to plasmonic lattice resonances: A collective directional source of polarized light. *Appl. Phys. Lett.* **2012**, *100*, 111103.
- (36) Lozano, G.; Louwers, D. J.; Rodríguez, S. R. K.; Murai, S.; Jansen, O. T. A.; Verschuuren, M. A.; Gómez Rivas, J. Plasmonics for solid-state lighting: enhanced excitation and directional emission of highly efficient light sources. *Light Sci. Appl.* **2013**, *2*, e66.
- (37) Zhou, W.; Dridi, M.; Suh, J. Y.; Kim, C. H.; Co, D. T.; Wasielewski, M. R.; Schatz, G. C.; Odom, T. W. Lasing action in strongly coupled plasmonic nanocavity arrays. *Nat. Nanotechnol.* **2013**, *8*, 506–511.
- (38) Lozano, G.; Grzela, G.; Verschuuren, M. A.; Ramezani, M.; Gómez Rivas, J. Tailor-made directional emission in nanoimprinted plasmonic-based light-emitting devices. *Nanoscale* **2014**, *6*, 9223–9229
- (39) Schokker, A. H.; Koenderink, A. F. Lasing at the band edges of plasmonic lattices. *Phys. Rev. B* **2014**, *90*, 155452.
- (40) Ramezani, M.; Lozano, G.; Verschuuren, M. A.; Gómez-Rivas, J. Modified emission of extended light emitting layers by selective coupling to collective lattice resonances. *Phys. Rev. B* **2016**, *94*, 125406.
- (41) Zakharko, Y.; Held, M.; Graf, A.; Rödlmeier, T.; Eckstein, R.; Hernandez-Sosa, G.; Hähnlein, B.; Pezoldt, J.; Zaumseil, J. Surface Lattice Resonances for Enhanced and Directional Electroluminescence at High Current Densities. ACS Photonics 2016, 3, 2225–2230.
- (42) Cotrufo, M.; Osorio, C. I.; Koenderink, A. F. Spin-Dependent Emission from Arrays of Planar Chiral Nanoantennas Due to Lattice and Localized Plasmon Resonances. *ACS Nano* **2016**, *10*, 3389–3397.
- (43) Schokker, A. H.; van Riggelen, F.; Hadad, Y.; Alù, A.; Koenderink, A. F. Systematic study of the hybrid plasmonic-photonic band structure underlying lasing action of diffractive plasmon particle lattices. *Phys. Rev. B* **2017**, *95*, 085409.
- (44) Wang, D.; Yang, A.; Wang, W.; Hua, Y.; Schaller, R. D.; Schatz, G. C.; Odom, T. W. Band-edge engineering for controlled multimodal nanolasing in plasmonic superlattices. *Nat. Nanotechnol.* **2017**, 12, 889.
- (45) Guo, R.; Nečada, M.; Hakala, T. K.; Väkeväinen, A. I.; Törmä, P. Lasing at K Points of a Honeycomb Plasmonic Lattice. *Phys. Rev. Lett.* **2019**, *122*, 013901.
- (46) Vaskin, A.; Kolkowski, R.; Koenderink, F. A.; Staude, I. Light-emitting metasurfaces. *Nanophotonics* **2019**, *8*, 1151.
- (47) Hu, J.; Wang, D.; Bhowmik, D.; Liu, T.; Deng, S.; Knudson, M. P.; Ao, X.; Odom, T. W. Lattice-Resonance Metalenses for Fully Reconfigurable Imaging. *ACS Nano* **2019**, *13*, 4613–4620.

- (48) Olson, J.; Manjavacas, A.; Basu, T.; Huang, D.; Schlather, A. E.; Zheng, B.; Halas, N. J.; Nordlander, P.; Link, S. High chromaticity aluminum plasmonic pixels for active liquid crystal displays. *ACS Nano* **2016**, *10*, 1108–1117.
- (49) Kristensen, A.; Yang, J. K. W.; Bozhevolnyi, S. I.; Link, S.; Nordlander, P.; Halas, N. J.; Mortensen, N. A. Plasmonic colour generation. *Nat. Rev. Mater.* **2017**, *2*, 16088.
- (50) Esposito, M.; Todisco, F.; Bakhti, S.; Passaseo, A.; Tarantini, I.; Cuscunà, M.; Destouches, N.; Tasco, V. Symmetry Breaking in Oligomer Surface Plasmon Lattice Resonances. *Nano Lett.* **2019**, *19*, 1922–1930.
- (51) Czaplicki, R.; Kiviniemi, A.; Laukkanen, J.; Lehtolahti, J.; Kuittinen, M.; Kauranen, M. Surface lattice resonances in second-harmonic generation from metasurfaces. *Opt. Lett.* **2016**, *41*, 2684–2687
- (52) Michaeli, L.; Keren-Zur, S.; Avayu, O.; Suchowski, H.; Ellenbogen, T. Nonlinear Surface Lattice Resonance in Plasmonic Nanoparticle Arrays. *Phys. Rev. Lett.* **2017**, *118*, 243904.
- (53) Huttunen, M. J.; Rasekh, P.; Boyd, R. W.; Dolgaleva, K. Using surface lattice resonances to engineer nonlinear optical processes in metal nanoparticle arrays. *Phys. Rev. A* **2018**, *97*, 053817.
- (54) Hooper, D. C.; Kuppe, C.; Wang, D.; Wang, W.; Guan, J.; Odom, T. W.; Valev, V. K. Second Harmonic Spectroscopy of Surface Lattice Resonances. *Nano Lett.* **2019**, *19*, 165–172.
- (55) Zou, S.; Schatz, G. C. Silver nanoparticle array structures that produce giant enhancements in electromagnetic fields. *Chem. Phys. Lett.* **2005**, 403, 62–67.
- (56) Nikitin, A. G.; Kabashin, A. V.; Dallaporta, H. Plasmonic resonances in diffractive arrays of gold nanoantennas: near and far field effects. *Opt. Express* **2012**, *20*, 27941–27952.
- (57) Huang, Y.; Ma, L.; Hou, M.; Zhang, Z. Universal Near-Field Interference Patterns of Fano Resonances in Two-Dimensional Plasmonic Crystals. *Plasmonics* **2016**, *11*, 1377–1383.
- (58) Guo, K.; Verschuuren, M. A.; Koenderink, A. F. Superresolution imaging of the local density of states in plasmon lattices. *Optica* **2016**, *3*, 289–298.
- (59) Manjavacas, A.; Zundel, L.; Sanders, S. Analysis of the Limits of the Near-Field Produced by Nanoparticle Arrays. *ACS Nano* **2019**, *13*, 10682–10693.
- (60) Rodriguez, S. R. K.; Abass, A.; Maes, B.; Janssen, O. T. A.; Vecchi, G.; Gómez Rivas, J. Coupling Bright and Dark Plasmonic Lattice Resonances. *Phys. Rev. X* **2011**, *1*, 021019.
- (61) Wang, D.; Wang, W.; Knudson, M. P.; Schatz, G. C.; Odom, T. W. Structural Engineering in Plasmon Nanolasers. *Chem. Rev.* **2018**, 118, 2865–2881.
- (62) Yang, A.; Hoang, T. B.; Dridi, M.; Deeb, C.; Mikkelsen, M. H.; Schatz, G. C.; Odom, T. W. Real-time tunable lasing from plasmonic nanocavity arrays. *Nat. Commun.* **2015**, *6*, 6939.
- (63) Hakala, T. K.; Rekola, H. T.; Väkeväinen, A. I.; Martikainen, J.-P.; Nečada, M.; Moilanen, A. J.; Törmä, P. Lasing in dark and bright modes of a finite-sized plasmonic lattice. *Nat. Commun.* **2017**, *8*, 13687.
- (64) Fernandez-Bravo, A.; Wang, D.; Barnard, E. S.; Teitelboim, A.; Tajon, C.; Guan, J.; Schatz, G. C.; Cohen, B. E.; Chan, E. M.; Schuck, P. J.; Odom, T. W. Ultralow-threshold, continuous-wave upconverting lasing from subwavelength plasmons. *Nat. Mater.* **2019**, *18*, 1172–1176.
- (65) Pourjamal, S.; Hakala, T. K.; Nečada, M.; Freire-Fernández, F.; Kataja, M.; Rekola, H.; Martikainen, J.-P.; Törmä, P.; van Dijken, S. Lasing in Ni Nanodisk Arrays. *ACS Nano* **2019**, *13*, 5686–5692.
- (66) Guo, K.; Koenderink, A. F. Spatial Intensity Distribution in Plasmonic Particle Array Lasers. *Phys. Rev. Applied* **2019**, *11*, 024025. (67) Taskinen, J. M.; Moilanen, A. J.; Rekola, H.; Kuntze, K.; Priimagi, A.; Törmä, P.; Hakala, T. K. All-Optical Emission Control and Lasing in Plasmonic Lattices. *ACS Photonics* **2020**, *7*, 2850–2858.
- (68) Guan, J.; et al. Quantum Dot-Plasmon Lasing with Controlled Polarization Patterns. ACS Nano 2020, 14, 3426–3433.

- (69) Laux, F.; Bonod, N.; Gérard, D. Single Emitter Fluorescence Enhancement with Surface Lattice Resonances. *J. Phys. Chem. C* **2017**, *121*, 13280–13289.
- (70) Hamans, R. F.; Parente, M.; Castellanos, G. W.; Ramezani, M.; Gómez Rivas, J.; Baldi, A. Super-resolution Mapping of Enhanced Emission by Collective Plasmonic Resonances. *ACS Nano* **2019**, *13*, 4514–4521.
- (71) Yadav, R. K.; Bourgeois, M. R.; Cherqui, C.; Juarez, X. G.; Wang, W.; Odom, T. W.; Schatz, G. C.; Basu, J. K. Room Temperature Weak-to-Strong Coupling and the Emergence of Collective Emission from Quantum Dots Coupled to Plasmonic Arrays. ACS Nano 2020, 14, 7347—7357.
- (72) Yadav, R. K.; Liu, W.; Li, R.; Odom, T. W.; Agarwal, G. S.; Basu, J. K. Room-Temperature Coupling of Single Photon Emitting Quantum Dots to Localized and Delocalized Modes in a Plasmonic Nanocavity Array. ACS Photonics 2021, 8, 576–584.
- (73) Yadav, R. K.; Otten, M.; Wang, W.; Cortes, C. L.; Gosztola, D. J.; Wiederrecht, G. P.; Gray, S. K.; Odom, T. W.; Basu, J. K. Strongly Coupled Exciton-Surface Lattice Resonances Engineer Long-Range Energy Propagation. *Nano Lett.* **2020**, *20*, 5043–5049.
- (74) Boddeti, A. K.; Guan, J.; Sentz, T.; Juarez, X.; Newman, W.; Cortes, C.; Odom, T. W.; Jacob, Z. Long-Range Dipole-Dipole Interactions in a Plasmonic Lattice. *Nano Lett.* **2021**, na.
- (75) Teperik, T. V.; Degiron, A. Design strategies to tailor the narrow plasmon-photonic resonances in arrays of metallic nanoparticles. *Phys. Rev. B* **2012**, *86*, 245425.
- (76) Lunnemann, P.; Koenderink, A. F. The local density of optical states of a metasurface. *Sci. Rep.* **2016**, *6*, 20655.
- (77) Kolkowski, R.; Koenderink, A. F. Lattice Resonances in Optical Metasurfaces With Gain and Loss. *Proc. IEEE* **2019**, 1–24.
- (78) HCubature Module by Steven G. Johnson. https://github.com/JuliaMath/HCubature.jl (accessed 2020-12-07).
- (79) Zundel, L.; Manjavacas, A. Finite-size effects on periodic arrays of nanostructures. *J. Phys.: Photonics* **2019**, *1*, 015004.
- (80) García de Abajo, F. J. Multiple scattering of radiation in clusters of dielectrics. *Phys. Rev. B* **1999**, *60*, 6086–6102.
- (81) Yang, H. U.; D'Archangel, J.; Sundheimer, M. L.; Tucker, E.; Boreman, G. D.; Raschke, M. B. Optical dielectric function of silver. *Phys. Rev. B* **2015**, *91*, 235137.
- (82) Auguié, B.; Bendaña, X. M.; Barnes, W. L.; García de Abajo, F. J. Diffractive arrays of gold nanoparticles near an interface: Critical role of the substrate. *Phys. Rev. B* **2010**, 82, 155447.
- (83) Zhou, W.; Odom, T. W. Tunable subradiant lattice plasmons by out-of-plane dipolar interactions. *Nat. Nanotechnol.* **2011**, *6*, 423.
- (84) Zhou, W.; Hua, Y.; Huntington, M. D.; Odom, T. W. Delocalized Lattice Plasmon Resonances Show Dispersive Quality Factors. J. Phys. Chem. Lett. 2012, 3, 1381–1385.
- (85) Huttunen, M. J.; Dolgaleva, K.; Törmä, P.; Boyd, R. W. Ultrastrong polarization dependence of surface lattice resonances with out-of-plane plasmon oscillations. *Opt. Express* **2016**, 24, 28279–28289.
- (86) Sanders, S.; Manjavacas, A. Analysis of the Limits of the Local Density of Photonic States near Nanostructures. *ACS Photonics* **2018**, *5*, 2437–2445.
- (87) Novotny, L.; Hecht, B. *Principles of Nano-Optics*; Cambridge University Press: New York, 2006.
- (88) Martín-Cano, D.; Martín-Moreno, L.; García-Vidal, F. J.; Moreno, E. Resonance Energy Transfer and Superradiance Mediated by Plasmonic Nanowaveguides. *Nano Lett.* **2010**, *10*, 3129–3134.
- (89) Abujetas, D. R.; Sánchez-Gil, J. A. Near-Field Excitation of Bound States in the Continuum in All-Dielectric Metasurfaces through a Coupled Electric/Magnetic Dipole Model. *Nanomaterials* **2021**, *11*, 998.
- (90) Bettles, R. J.; Gardiner, S. A.; Adams, C. S. Enhanced Optical Cross Section *via* Collective Coupling of Atomic Dipoles in a 2D Array. *Phys. Rev. Lett.* **2016**, *116*, 103602.
- (91) Shahmoon, E.; Wild, D. S.; Lukin, M. D.; Yelin, S. F. Cooperative Resonances in Light Scattering from Two-Dimensional Atomic Arrays. *Phys. Rev. Lett.* **2017**, *118*, 113601.

- (92) Guimond, P.-O.; Grankin, A.; Vasilyev, D. V.; Vermersch, B.; Zoller, P. Subradiant Bell States in Distant Atomic Arrays. *Phys. Rev. Lett.* **2019**, *122*, 093601.
- (93) Alaee, R.; Gurlek, B.; Albooyeh, M.; Martín-Cano, D.; Sandoghdar, V. Quantum Metamaterials with Magnetic Response at Optical Frequencies. *Phys. Rev. Lett.* **2020**, *125*, 063601.
- (94) Rui, J.; Wei, D.; Rubio-Abadal, A.; Hollerith, S.; Zeiher, J.; Stamper-Kurn, D. M.; Gross, C.; Bloch, I. A subradiant optical mirror formed by a single structured atomic layer. *Nature* **2020**, *583*, 369–374.
- (95) Capolino, F.; Jackson, D. R.; Wilton, D. R.; Felsen, L. B. Comparison of Methods for Calculating the Field Excited by a Dipole Near a 2-D Periodic Material. *IEEE Trans. Antennas Propag.* **2007**, *55*, 1644–1655.

